POLITECNICO DI TORINO
Repository ISTITUZIONALE

Synergetic Application of Zero-, One-, and Three-Dimensional Computational Fluid Dynamics Approaches for Hydrogen-Fuelled Spark Ignition Engine Simulation

(Article begins on next page)

26 December 2024

Synergetic Application of Zero-, One-, and Three-Dimensional Computational Fluid Dynamics Approaches for Hydrogen-Fuelled Spark Ignition Engine Simulation

Federico Millo,[1] **Andrea Piano,**[1] **Luciano Rolando,**[1] **Francesco Accurso,**[1] **Fabrizio Gullino,**[1] **Salvatore Roggio,**[1] **Andrea Bianco,**[2] **Francesco Pesce,**[3] **Alberto Vassallo,**[3] **and Riccardo Rossi**[4]

[1]Politecnico di Torino, Italy
[2]Powertech Engineering, Italy
[3]PUNCH Torino, Italy
[4]PUNCH Hydrocells, Italy

Abstract

Nowadays hydrogen, especially if derived from biomass or produced by renewable power, is rising as a key energy solution to shift the mobility of the future toward a low-emission scenario. It is well known that hydrogen can be used with both internal combustion engines (ICEs) and fuel cells (FCs); however, hydrogen-fuelled ICE represents a robust and cost-efficient option to be quickly implemented under the current production infrastructure. In this framework, this article focuses on the conversion of a state-of-the-art 3.0L diesel engine in a hydrogen-fuelled Spark Ignition (SI) one. To preliminarily evaluate the potential of the converted ICE, a proper simulation methodology was defined combining zero-, one-, and three-dimensional (0D/1D/3D) Computational Fluid Dynamics (CFD) approaches. First of all, a detailed kinetic scheme was selected for both hydrogen combustion and Nitrogen Oxides (NOx) emission predictions in a 3D-CFD environment. Afterward, to bring the analysis to a system-level approach, a 1D-CFD predictive combustion model was firstly optimized by implementing a specific laminar flame speed correlation and, secondly, calibrated against the 3D-CFD combustion results. The combustion model was then integrated into a complete engine model to assess the potential benefit derived from the wide range of flammability and the high flame speed of hydrogen on a complete engine map, considering NOx formation and knock avoidance as priority parameters to control. Without a specific modification of turbocharger and combustion systems, a power density of 34 kW/L and a maximum brake thermal efficiency (BTE) of about 42% were achieved, thus paving the way for further hardware optimization (e.g., compression ratio reduction, turbocharger optimization, direct injection [DI]) to fully exploit the advantages enabled by hydrogen combustion.

1

Introduction

The huge climate changes observed in the last decades as a consequence of Greenhouse Gases (GHG) emissions boosted the efforts of the European Union (EU) to decarbonize its economy. As a matter of fact, with the European Green Deal announced by the European Commission at the end of 2019 [1], the EU aims to achieve climate neutrality by 2050. In such a framework, particular attention is devoted to the shift toward more sustainable mobility since the transportation sector is responsible for 25% of the total CO_2 emissions and, differently from other relevant sectors, has shown an increasing trend in the past 25 years [2]. Besides the fostering of powertrain electrification, which represents the most promising solution to improve the air quality in highly congested urban areas, the European Green Deal also supports the development and the production of sustainable alternative fuels capable to achieve a zero impact in their entire life cycle [3]. Among them, hydrogen has recently become a highly attractive solution since it could be produced from renewable energy sources, and its combustion generates no GHG emissions. In this context, the European Commission initiated a new dedicated strategy on hydrogen in Europe [4], simultaneously launching the European Clean Hydrogen Alliance [5], aiming to assist in large scale the deployment of hydrogen technologies and infrastructures by 2030.

Although hydrogen may be at first associated with Fuel Cell (FC) applications [6], its use as fuel in Internal Combustion Engines (ICEs) represents a very attractive option [7, 8]. The advantages of hydrogen ICE compared to the FC technology include a higher tolerance to fuel impurities, reduction of rare materials usage, and a more straightforward transition from conventional vehicles [9]. In fact, H_2-ICE technology benefits from the reduced production cost of using the existing mature manufacturing facilities and processes for conventional ICEs. Finally, from a thermodynamic point of view, the physical properties of H_2 allow an excellent combustion quality. As a matter of fact, hydrogen, in comparison to other fuels, features a high Lower Heating Value (LHV) (i.e., H_2 = 120 MJ/kg vs Gasoline = 44.1 MJ/kg [10]), and fast flame propagation over a wide range of temperature, pressure, and air-to-fuel ratios [7]. Therefore, highly lean operations in combination with fast and optimally phased combustion results in a high energy conversion efficiency and in very low Nitrogen Oxides (NOx) emissions thanks to low burning temperature [11]. On the other side, the combination of the low H_2 density and lean mixture may limit the specific power output of the engine or create huge challenges for the design of the charging system [12, 13]. From the abnormal combustion perspective, the high values of both autoignition temperature and octane number of hydrogen can limit the knock likelihood. However, the low minimum ignition energy (about 0.016 mJ [13]) may strongly increase the risk of preignition, glow ignition, and backfiring in the case of external mixture preparation [14]. Finally, the high diffusion coefficient of H_2 leads to fast mixing with the induced air (compared to conventional fuels), which is beneficial for mixture homogenization in the case of Port Fuel Injection (PFI) engines but could be detrimental for stratified Direct Injection (DI) engines.

Despite the first studies were carried out at the beginning of the twentieth century, only in the last decade the growing demand for a decarbonized mobility, together with the tightening of the emission standards, and the development of renewable hydrogen technologies have increased the global interest toward hydrogen powertrains [15, 16]. Besides the activities of automotive manufacturers which are investigating the feasibility of hydrogen propelled vehicles through the development of several prototypes for both passenger cars and heavy-duty (HD) applications [17, 18, 19], a huge number of research projects is currently ongoing to identify the most attractive hydrogen powertrain solutions [20]. As a matter of fact, scientific literature presents a wide range of possible H_2 applications relying on either fuel autoignition [21], Dual Fuel concepts [22, 23], or premixed combustion. In such a framework, Spark Ignition (SI) engines represent the most common solution with studies on both PFI and DI systems. Despite DI configurations are able to achieve better performance thanks to the higher volumetric efficiency [24] and the lower risk of abnormal combustion [14], PFI may represent the preferred midterm solution to boost the diffusion of new H_2 engines, limiting, at the same time, the initial investments and the additional costs [20, 25]. Indeed, they do not require the development of new components (e.g., high-pressure injectors) [26], and they can be easily derived from existing units propelled with conventional fuels. For example, Koch et al. [25] have proved that the revamping could be performed also with diesel engines since the spark plug can be installed in the cylinder head through the machining of the injector seat. Moreover, the presence of the Exhaust Gas Recirculation (EGR) loop, mandatory in the latest generation of compression ignition engines, may enable additional strategies to reduce pumping losses, NOx emissions, and the occurrence of abnormal combustion phenomena. Finally, the use of a turbocharger may allow to overcome the limitations on the engine power output even if the poor volumetric efficiency of PFI configurations in combination with highly lean operations generate several challenges in the design of the charging system [2, 27].

To preliminarily assess the performance of H_2 engines, despite several research projects only relying on experimental activities [12, 27], the exploitation of numerical tools is crucial to fully understand the fundamentals of both mixture preparation [28] and combustion process [29] and to perform a comprehensive optimization of the system. Klepatz et al. [13] presented a combined approach where the one-dimensional (1D) Computational Fluid Dynamics (CFD) model of the H_2-ICE has been primarily validated against a set of experimental data and then used to compare the efficiency of different engine concepts. In a subsequent work [25], the same methodology has been exploited to optimize the calibration of a diesel-revamped H_2 engine and to assess the benefit of EGR on its performance and emissions. Scarcelli et al. also proposed a similar synergic approach: the results of an experimental campaign on a single-cylinder optical engine fuelled with hydrogen have been used to validate a three-dimensional

(3D)-CFD model [30] through which several sensitivity analyses on the injector geometry and of injection parameters have been performed [31]. Nevertheless, for such innovative ICE, experimental data for model validation are quite often not available, and the simulation of such an alternative fuel places several challenges related to the presence of supersonic jets [32], to the correct estimation of the burning speed [33, 34], and to the prediction of the abnormal combustion phenomena [35]. In such a framework, the development of a reliable simulation tool capable to preliminarily assess the potential of the hydrogen-fuelled engine and to drive its design in the early stage of the development process is to be of paramount importance especially when experimental data are lacking. To tackle this task, this article aims to provide a comprehensive methodology to assess, through numerical simulations, the performance of a Hydrogen SI ICE revamped from a state-of-the-art turbocharged Common Rail (CR) diesel engine. This methodology was exploited for the preliminary assessment of the H_2-ICE potential employed on a hybrid bus for urban applications [36].

After a short description of the tested engine, the article presents the hierarchical 0D/1D/3D approach for the simulation of a hydrogen engine. Primarily the 3D simulation setup is deeply analyzed proving its capabilities to catch the impact of charge dilution and Spark Timing (ST) on the combustion development. Afterward, the main features of the 1D combustion model and its calibration against the 3D-CFD results are presented. The last part of the article deals with the optimization of the engine calibration parameter: primarily the setup of the virtual test rig is described, paying particular attention to the target and the constraints of the study. Then the outcomes of the optimization process represented by the maps of the main operating parameters are discussed. Finally, two sensitivity analyses on the compression ratio and the turbocharger size are shown to prove the capabilities of the proposed methodology to drive the design of the engine architecture and not only to optimize its operating parameters.

Case Study

A state-of-the-art low compression ratio, 3.0L multicylinder diesel engine architecture was selected as a case study. The combustion system conversion from diesel to hydrogen was divided into two main steps: first of all, a centrally mounted spark plug was properly adapted in the original diesel injector location, keeping unchanged the original flat cylinder head; secondly, PFI system coupled with original highly reentrant diesel bowl, was adopted to demonstrate the target achievement with the minimum level of cost and complexity. The original diesel engine block and the swirl-based cylinder head were kept unchanged to meet the main requirements of the retrofit application, but the adaptation of its compression ratio through a specific cylinder head gasket thickness was also considered to increase the knock margin of the engine at high loads. Additional details related to specific engine features cannot be disclosed due to confidentiality reasons. Figure 1 shows the selected combustion system.

The selection of PFI configuration for H_2 injection has implied a properly redesigned of the intake system to comply with two port fuel injectors, one for each intake port. The main characteristics of the hydrogen injection system are reported in Table 1.

As far as the boosting system is concerned, even if the adoption of PFI configuration reduces the engine volumetric efficiency due to the low density of the gaseous H_2 injection in the intake port, the original turbocharger system (featuring a Variable Geometry Turbine, VGT) was selected for a preliminary performance estimate. However, taking into account the intake air reduction and the lean and fast combustion induced by H_2, thus resulting in low temperature at turbine inlet, a proper turbocharger was defined and its potentials in terms of power density improvements will be reported later in the manuscript. The air path modification consisted also of the introduction of a throttle valve at the Charge Air Cooler (CAC) outlet since throttling operation is needed at low loads to reduce the intake air, without increasing the risk of combustion instabilities. Although additional benefits in terms of in-cylinder flow field intensity could be achieved with an optimization of the valve timing or adopting a variable valve actuation, the original valve timing, both for intake and exhaust valves, was considered to assess the performance with a limited conversion complexity.

The original high-pressure EGR path was modified by introducing an EGR cooler to recirculate cooled exhaust gas into the intake manifold. However, the increment of charge temperature at the intake manifold can lead to H_2 autoignition in the combustion chamber, especially at high loads. Therefore, in this application, EGR has been used to increase charge dilution and to control combustion and NOx emission levels at low-medium engine loads.

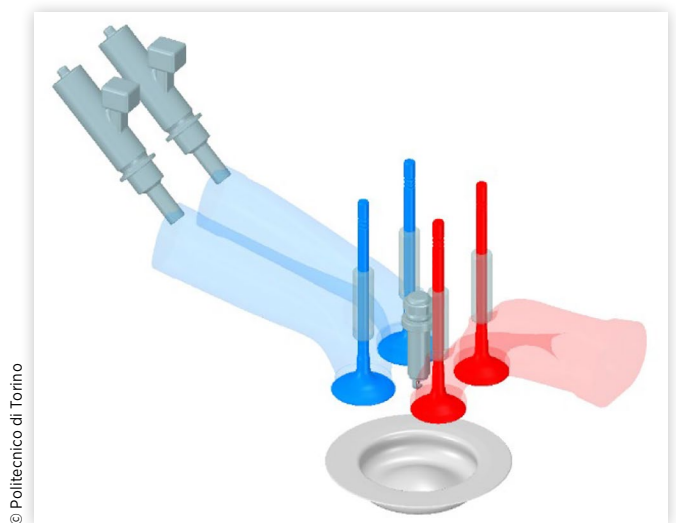**FIGURE 1** Selected architecture for combustion system conversion from diesel to H_2 engine.

© Politecnico di Torino

TABLE 1 Main characteristics of the hydrogen PFI system.

Maximum rail pressure	1000 kPa
Maximum static H_2 flow	>1.4 g/s
Minimum dynamic H_2 flow	0.06 g/s
Maximum ET at maximum speed	30 ms at 4000 RPM
H_2 temperature range	No temperature conditioning
Maximum tank pressure	700 bar

© Politecnico di Torino

Simulation Methodology

As well known, numerical simulation, with both detailed 3D-CFD and system-level 1D-CFD approaches, is commonly used in the engine concept design phase to reduce costly and time-consuming experimental investigations thanks to its high predictive capabilities and affordable computational times with the actual Central Processing Unit (CPU) power. In this scenario, the proposed architecture (depicted in Figure 1) was investigated by means of a dedicated 0D/1D/3D-CFD synergetic approach with the aim of capturing and reproducing the hydrogen combustion characteristics. A 3D-CFD numerical setup based on a detailed chemistry scheme was defined, and its outcomes were used as a reference for calibrating a predictive combustion model in a 1D-CFD environment, necessary for a preliminary assessment of the engine operating maps for the selected architecture. In addition, 0D autoignition calculations, based on the above-mentioned detailed chemistry scheme, were used for a preliminary system-level knock risk evaluation. To properly reproduce the hydrogen combustion peculiarities and to address the consequent calibration of the quasi-dimensional combustion model, several engine operating conditions, in terms of Brake Mean Effective Pressure (BMEP) and engine speed, were selected. In addition, dilution rate, both in terms of EGR and relative air-to-fuel ratio (lambda), and ST were swept, as highlighted in Table 2, to exploit the complete wide flammability range of H_2. The target load, the dilution, and spark

TABLE 2 Engine operating conditions test matrix.

Engine speed [RPM]	Target BMEP [bar]	Lambda [—]	EGR [%]	ST [CA deg aTDCf]
2000	2.0	1.8	30	−25
		2.35	22	−24
		2.5	5	−20
	4.0	2.1	30	−30
		2.35	22	−30
		2.45	5	−25.4
	8.0	2.3	0	−16.5
		2.3	0	−8.5
		2.3	15	−28
		2.3	15	−20
3000	8.0	2.3	10	−20
		2.5	0	−16.4
3500	10.0	2.3	0	−2.5

© Politecnico di Torino

advance levels were obtained from preliminary 1D-CFD calculations that relied on combustion assumptions from the available literature.

3D-CFD Simulation Environment

The first step of the multidimensional simulation methodology was the 3D-CFD analysis, which was carried out in commercially available software, CONVERGE CFD v3.0 [37]. To properly initialize the computational domain, a preliminary 1D-CFD complete engine model was built in GT-SUITE, providing the time-dependent boundary conditions for pressure, temperature, and species concentrations. As far as numerical schemes are concerned, a second-order central difference scheme for spatial discretization and a first-order implicit Euler scheme for temporal discretization were selected, with a variable time-step size that assured the minimization of simulation time without affecting simulation accuracy. The Navier-Stokes conservation equations were solved through the Pressure Implicit with Splitting Operator (PISO) algorithm of Issa [38] coupled with the Rhie-Chow scheme for pressure-velocity coupling [39]. After a mesh grid sensitivity analysis, not reported in the herein study for the sake of brevity, a base grid size equal to 2 mm was chosen. Moreover, adopting several user-defined mesh refinements, as fixed embedding and Adaptive Mesh Refinement (AMR) techniques [40], a minimum grid size of 0.25 mm was reached. The resulting mesh grid can be considered consistent with previous computational studies on similar engine applications [28, 41]. Regarding turbulence modelling, the Reynolds-Averaged Navier-Stokes (RANS)-based Re-Normalization Group (RNG) k-ε model [42] was used since it is capable to account for flame-induced compression, expansion, and rapid strain effects on the turbulent quantities [43] without any specific modification on thermal and diffusive model constants (turbulent Prandtl and Schmidt numbers). Kinematic and thermal boundary layers were described by means of law of the walls [44], featuring standard wall functions and fixed embedding for wall mesh refinement. Additionally, the O'Rourke and Amsden model [45] was set for the turbulent heat transfer prediction.

Concerning combustion modelling, in recent years different research activities on SI engines have been focused on the Well-Stirred Reactor (WSR) assumption showing encouraging results [46, 47, 48]. This approach guarantees an accurate combustion prediction relying on a proper chemical reaction mechanism, avoiding the calibration of dedicated model constants that usually requires experimental data, not available in preliminary investigations as the herein study. Moreover, typical engine operating conditions when hydrogen is used as a fuel exploit lean mixture thanks to the wide flammability range and high laminar flame speed of H_2. In these conditions, the combustion regime may go outside the "flamelet" assumption, as widely reported in [49, 50], confirming the WSR approach as the best solution to properly predict the combustion process. Considering all the above, in

© Politecnico di Torino

TABLE 3 Reaction mechanism features.

Fuel species	H_2
Species	44
Reactions	234
H_2/O_2 submech	Kéromnès et al. [52]
NOx submech	Embedded in the reaction mechanism

© Politecnico di Torino

this study the SAGE detailed chemistry combustion model [40], which is based on WSR assumption, was adopted. A comprehensive sensitivity analysis was carried out to select the most appropriate reaction mechanism. The one proposed by Zhang et al. [51] (44 species and 234 reactions) was selected since it considers significant updates related to hydrogen and NOx reactions. More in detail, the hydrogen submechanism is based on the previously developed Kéromnès et al. [52] reaction mechanism, which has shown the lowest error both for ignition delay and flame velocity prediction among several reaction mechanisms for hydrogen combustion [53]. The main features of the reaction mechanism used in this study are listed in Table 3.

To deeper investigate the importance of each chemical reaction to the mixture reactivity, 0D constant volume simulations were carried out in CONVERGE CFD v3.0 for the selected reaction mechanism by means of the adjoint sensitivity analysis [40, 54]. Indeed the sensitivity analysis shows how a variation of reaction rate constants determines a change of temperature, which can be considered a suitable indicator of the contribution of each chemical reaction to the overall reactivity. Figure 2 shows the normalized sensitivity coefficients of the 9 most relevant reactions for lambda 2.3-EGR 0% mixture conditions at 850 K and three different pressure values (15, 30, and 60 bar), considered as representative of typical engine operating conditions at the end of compression.

FIGURE 2 Normalized sensitivity coefficients for the 9 most sensitive reactions, at 850 K; 15 bar, 30 bar, 60 bar; lambda 2.3; and EGR 0%.

© Politecnico di Torino
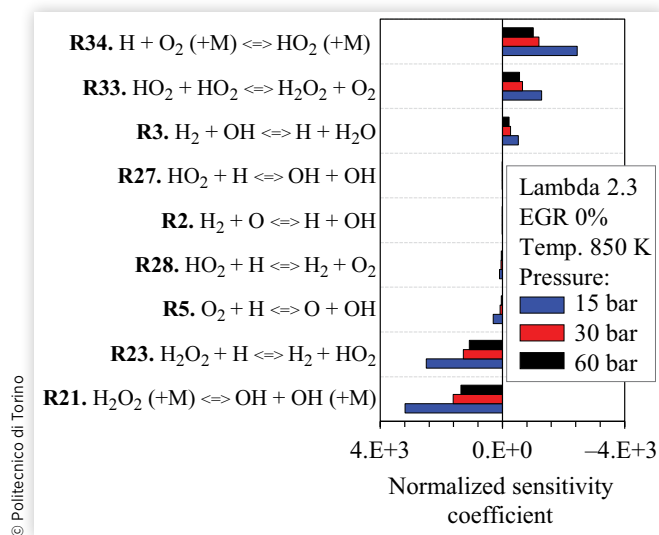
High sensitivity coefficients can be highlighted for reactions R21 and R23 suggesting that the reactivity of the mixture is mainly controlled by the reactions involving the production and consumption of H_2O_2. R21 and R23 are counterbalanced by the R33 chain-terminating reaction, which consumes two HO_2 radicals producing H_2O_2. Increasing the pressure, R21 and R23 remain the most sensitive reactions, suggesting that the H_2O_2 can be considered as a suitable tracer of preflame reactions and autoignition. This is also confirmed by the study of Kéromnès et al. [52], in which the thermal decomposition of H_2O_2 was found to be the dominant chain-branching reaction for hydrogen ignition, at high pressure and intermediate temperature conditions.

In this preliminary analysis, 3D-CFD simulations were used as a reference for the analysis of H_2 combustion and the subsequent calibration of the 0D/1D combustion model. Indeed thanks to the developed 3D-CFD simulation setup, the impact of the retrofit reentrant piston bowl on flame/wall interaction and the effects of different engine calibration, both in terms of dilution rate and ST, were evaluated. In this regard, to understand the effect of the combustion system on flame velocity and the dilution rate tolerance, the in-cylinder flame evolution was investigated at 2000 RPM and high-load operating conditions, where the high turbulence induced by the intake stroke affects the combustion rate as well. Firstly, the combustion process was analyzed under a high relative air-to-fuel ratio and without EGR (Case#1: lambda 2.3-EGR 0%). Then the dilution rate was increased, adopting an EGR = 15%. For this latter engine calibration, two different STs were considered, one equal to Case#1 (Case#2: lambda 2.3-EGR 15%), while the other 11 deg earlier (Case#3: lambda 2.3-EGR 15%-early ST). Figure 3(a) shows the in-cylinder pressure and the Heat Release Rate (HRR) for each engine calibration under investigation. At constant ST, the increment of EGR rate results in a slower combustion duration, as clearly highlighted by the comparison between Case#2 and Case#1. To speed up and to make the combustion process again efficient, the advanced ST was adopted (Case#3): in this case, a comparable combustion duration is reached in comparison with Case#1 thanks to the high laminar flame speed of hydrogen even considering an increment of the dilution rate.

The in-cylinder flame evolution was investigated in terms of temperature and distribution of H_2O_2 cylinder mass fraction (yH_2O_2). Figure 3 shows the temperature (plane A) and yH_2O_2 (plane B) distributions at each crank angle degrees after the ST (deg aST) highlighted in Figure 3(a) (i.e., θ_1, θ_2, θ_3). At θ_1 = +15 deg aST [Figure 3(b)], increasing the EGR rate (Case#2) results in lower flame temperature and slower flame propagation with respect to Case#1 due to the increment of dilution level within the combustion chamber, which reduces both the flame radius and the flame temperature. With early ST (Case#3), a slightly lower flame radius can be observed with respect to Case#2 due to the reduced temperature at the ignition. Moving ahead in the combustion process, at θ_2 = +23 deg aST [Figure 3(c)], the flame front of Case#1 reaches the piston bowl rim and propagates toward the cylinder liner in the reduced volume of the squish region thanks to the high laminar flame speed of hydrogen which reduces the flame

FIGURE 3 Combustion evolution among different dilution rates and STs. Plane A: temperature contour plot. Plane B: H_2O_2 mass fraction distribution. Left (Case#1): lambda 2.3-EGR 0%; middle (Case#2): lambda 2.3-EGR 15%; right (Case#3): lambda 2.3-EGR 15%-early ST. Engine operating condition of 2000 RPM at a high load.


© Politecnico di Torino
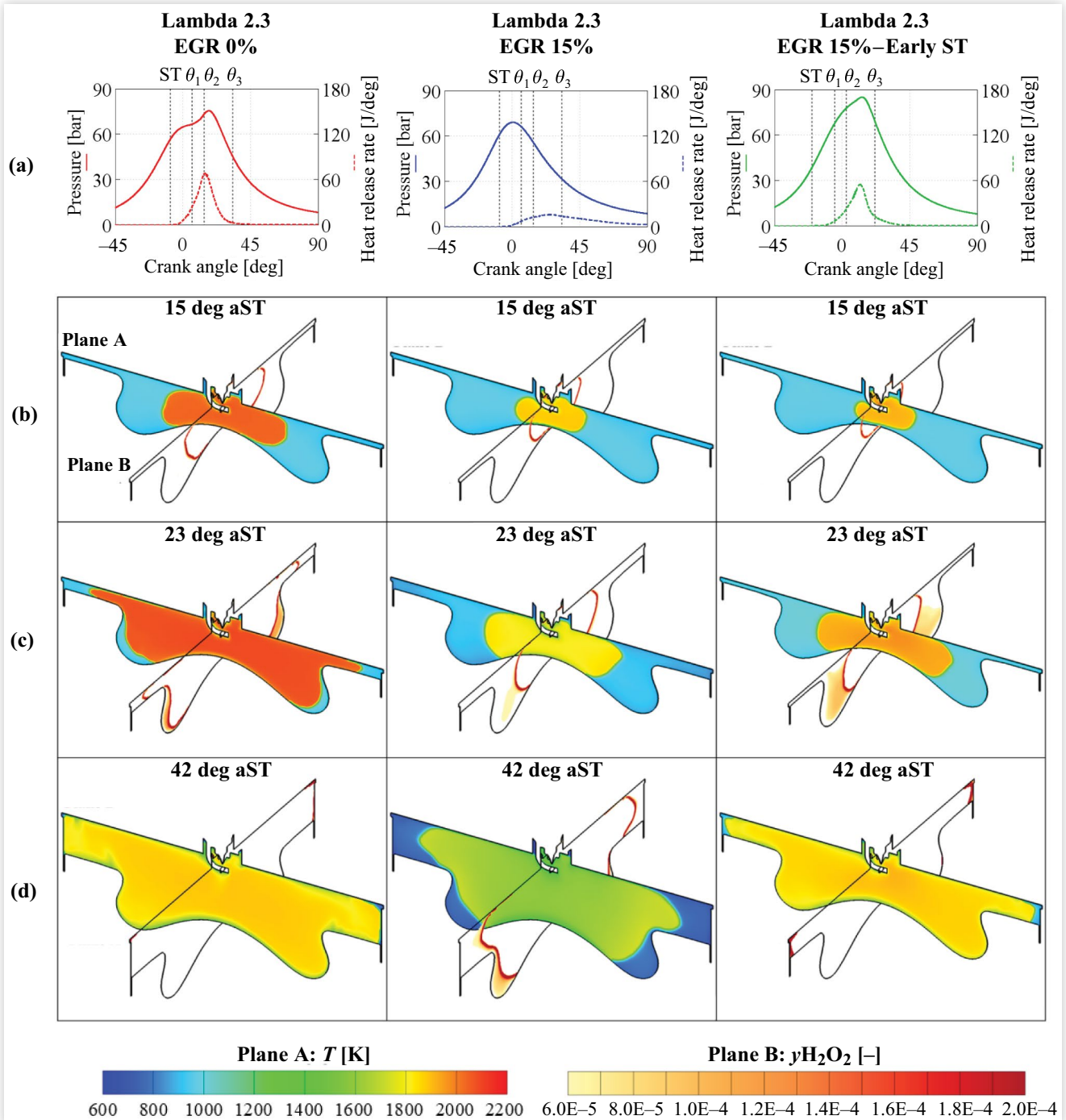
thickness. At this stage, the HRR exhibits its maximum value, then reduces its intensity due to heat transfer and to the flame propagation hindered by the geometry of the squish region. The cases with higher EGR (Case#2 and Case#3) show a similar flame propagation; however, the advanced ST calibration results in higher unburned temperature, and thus, a higher flame velocity could be expected later in the cycle. In the late combustion phase, at θ_3 = +42 deg aST, the flame front reaches the liner for Case#1, as highlighted by the yH_2O_2 distribution of Figure 3(d). The high diffusivity of hydrogen can overcome the geometric obstacle for the flame propagation, thus suggesting the possibility to implement without any modification a diesel-like combustion system, even with a reduced squish height. However, as expected, the increased dilution rate leads to a slower combustion process, as highlighted for Case#2 by yH_2O_2 distribution placed near the bowl rim due to an attenuated flame propagation in the squish region. Thanks to the advanced ST (Case#3), the flame almost reaches the liner, resulting in a similar combustion duration with respect to Case#1.

As already highlighted in the results of the adjoint sensitivity and confirmed by Figure 3, the highest magnitude of yH_2O_2 is localized in the flame front, where a rapid temperature change can be detected due to the combustion progress. In addition, the yH_2O_2 magnitude in the flame front appears quite similar among different dilution rates, despite the different chemical compositions of the charge. Therefore, the flame front can be traced with high accuracy through the definition of a certain yH_2O_2 distribution threshold. Thanks to this methodology, different characteristic quantities of the combustion process can be detected, such as the relative air-to-fuel ratio on the flame front, which is crucial for the analysis of H_2 DI concepts and design, as well as for 1D-CFD combustion prediction under non-premixed combustion. In this study, the flame location was evaluated by averaging the flame radius in the region with the highest magnitude of yH_2O_2 to quantitatively evaluate the combustion progress. Figure 4 shows the resulting average flame radius for the same engine calibrations previously investigated in Figure 3, having as a reference for the start of the analysis the relative ST.

As expected, Case#1 shows a higher flame speed than the cases with a higher EGR rate (Case#2 and Case#3). In particular, the average flame radius reaches the liner even considering the attenuated propagation in the squish region, represented by the slope change close to the dashed line that represents the liner location.

Increasing the EGR rate (Case#2), a significant flame speed reduction can be detected, with the flame that does not reach the liner even 45 deg aST. However, as already pointed out, the flame propagation slowdown can be avoided by advancing the ST (Case#3). More specifically, during the first stage of the combustion process, the flame shows a reduced propagation radius in comparison with Case#1 due to the increased dilution and reduced mixture temperature at the ST. Indeed, Case#3 shows a lower average flame radius than Case#2 up to +20 deg aST, thus confirming the combined effect of EGR and not optimal thermodynamic conditions on the flame propagation. Then the increased flame temperature for early ST speeds up the combustion progress, highlighting a similar flame propagation speed of Case#1.

FIGURE 4 Average flame radius among different dilution rates and STs. Engine operating condition of 2000 RPM at a high load.

© Politecnico di Torino
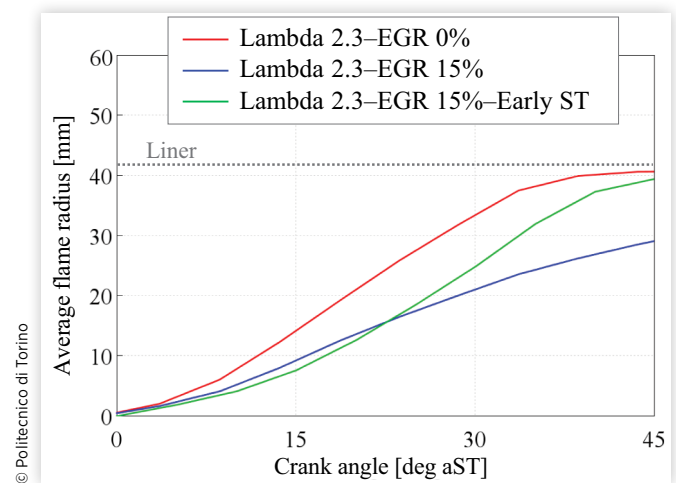
1D-CFD Simulation Environment

Combustion and Emissions Modelling In view of the results obtained through 3D-CFD analysis, the proper simulation of the combustion process plays a crucial role if the reliable predictions of engine power, fuel, and air consumption have to be performed within a system-level simulation framework. In this regard, this section focuses on the development of a 1D-CFD combustion model in a GT-SUITE simulation environment for the hydrogen combustion simulation. The recent works available in the literature concerning the simulation of the combustion process for H_2-air mixture showed both numerical approaches [13, 55, 56] and phenomenological models [57, 58] to address this objective. However, the absence of an extensive experimental dataset concerning the application of H_2 in ICEs, which is needed to properly calibrate a numerical combustion model (e.g., Wiebe function), made the numerical approach unsuitable and guided the authors toward the adoption of phenomenological models. Indeed 0D/1D phenomenological predictive combustion models can accurately reproduce the combustion process even considering a limited dataset of experimental data or 3D-CFD detailed simulations, as in the herein study. Therefore, the SITurb predictive combustion model available in GT-SUITE was considered for the hydrogen combustion simulation. This combustion model was successfully exploited in several case studies available in the literature, especially for gasoline SI engines [59, 60]. It is a two-zone combustion model capable to simulate the HRR in a spark-ignited combustion process characterized by a turbulent propagating flame. The turbulent flame brush is modelled via a spherical propagation and with a typical entrainment and burn-up approach, where the flame wrinkling effect is captured by the turbulent flame speed [61]. More in detail, the entrained mass (M_e) rate of the unburned air-fuel mixture in the flame front is dependent on the flame area (A_f), the unburned gas density (ρ_u), and the sum of the

turbulent and laminar flame speeds (S_T and S_L, respectively), as expressed by Equation 1:

$$\frac{dM_e}{dt} = \rho_u A_f \left(S_T + S_L \right) \qquad \text{Eq. (1)}$$

Besides, Equation 2 is used to determine the burn rate:

$$\frac{dM_b}{dt} = \frac{M_e - M_b}{\tau} \qquad \text{Eq. (2)}$$

where τ is assumed to be the time needed by the laminar flame speed to cover the Taylor microscale (λ) of turbulence, which depends on the turbulence integral length scale (L_i) and on Reynolds number (Re_t), as expressed by Equation 3.

$$\tau = \frac{\lambda}{S_L} = C_{TLS} \frac{L_i}{\sqrt{Re_t}} \frac{1}{S_L} \qquad \text{Eq. (3)}$$

C_{TLS} is a tuning parameter that can be used to adjust the burn rate of the unburned mass entrained in the flame brush. Both laminar and turbulence flame speed are evaluated by the software according to empirical formulations, which can be optimized to properly consider the burning properties of the fuel involved in the combustion process. Since hydrogen is characterized by flammability properties drastically different from conventional fuels, a specific and accurate correlation of the laminar flame speed model was defined. In line with a recent work by Rezaei et al. [57], in the herein study a specific laminar flame speed model for the hydrogen-air combustion was developed and correlated against detailed chemistry 1D-CFD calculations carried out by means of CONVERGE CFD software. The detailed Zhang et al. mechanism [62], used for the previously described extensive 3D-CFD analysis, was employed as a reaction scheme to preserve the consistency of the proposed methodology. A wide range of thermodynamic and mixture properties was evaluated for the laminar flame speed model development, covering from stoichiometric to ultra-lean hydrogen-air mixture at engine-relevant pressures and temperatures, as well as considering up to 30% of burned gas mass concentration. The simulation matrix is reported in Table 4, resulting in more than 1600 different operating conditions.

The laminar flame speed equation, defined as a power-law formulation, is presented in Equation 4.

$$S_L \left(\phi, T_u, p_u, x_b \right) = S_{L0} \left(\frac{T_u}{T_0} \right)^{\alpha} \left(\frac{p_u}{p_0} \right)^{\beta} \left(1 - \gamma x_b \right) \qquad \text{Eq. (4)}$$

where S_{L0} is the velocity evaluated at $T_u = T_0 = 298\,\text{K}$, $p_u = p_0 = 1\,\text{atm}$, and without burned gas ($x_b = 0$), while α, β, and γ are coefficients that consider the sensitivity of the laminar flame speed to the

TABLE 4 Simulation matrix considered for the 1D-CFD detailed chemistry laminar flame speed and induction time calculations.

	Minimum	Maximum
Equivalence ratio [—]	0.2	1
Unburned temperature [K]	600	1100
Pressure [bar]	10	120
Burned gas content [%]	0	30

© Politecnico di Torino

temperature, pressure, and residual gasses, respectively. This laminar flame speed formulation has been widely adopted by many researchers for different fuels [63]. As far as the S_{L0} is concerned, the approach proposed by Verhelst and Sierens [64] has been adopted in this work: the laminar flame speed at T_0 and p_0 was expressed by means of a fifth-order polynomial function, which depends on the equivalence ratio, as reported in Equation 5:

$$S_{L0}(\phi) = a_5 \phi^5 + a_4 \phi^4 + a_3 \phi^3 + a_2 \phi^2 + a_1 \phi + a_0 \qquad \text{Eq. (5)}$$

Moving to α, β, and γ coefficients, a second-order polynomial expression upon the equivalence ratio was selected for all these parameters and tuned to minimize the deviation from the 1D-CFD calculations. For the sake of conciseness, the optimized parameter set of the proposed laminar flame speed correlation is reported in the Appendix of this manuscript. A satisfactory agreement between the developed model and the laminar burning velocity computed with the Zhang et al. detailed kinetic scheme was obtained, as depicted in the correlation plot in Figure 5, considering more than 1600 different operating conditions of Table 4. An average error close to 7% was reached, with R2 = 0.97. The extended validation confirms the high accuracy level reached by the developed correlation, thus successfully overcoming one of the main issues in hydrogen combustion simulation. More details can be found in the Appendix, where a comprehensive comparison between the detailed chemistry 1D calculations and the result of the optimized model is reported.

Moving to the turbulence flame speed evaluation, the standard function implemented in GT-SUITE was used, as reported in Equation 6:

$$S_T = C_{TFS} u' \left(1 - \frac{1}{1 + C_{FKG} \left(\frac{R_f}{L_T} \right)^2} \right) \qquad \text{Eq. (6)}$$

FIGURE 5 Correlation plot between detailed chemistry laminar flame speed calculations and laminar flame speed values predicted by the developed model.
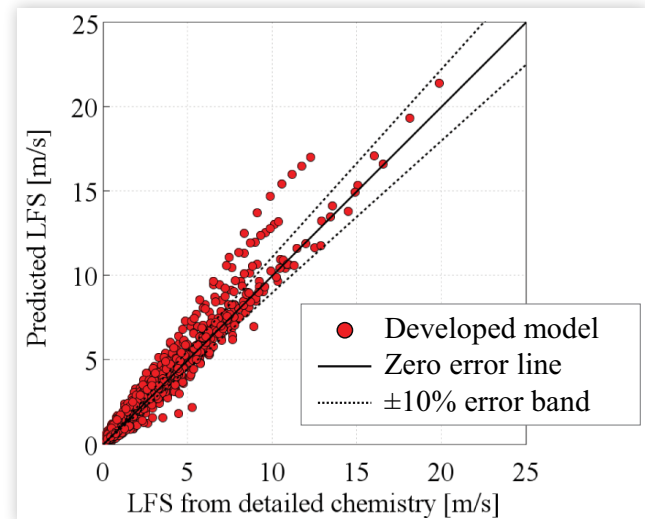

© Politecnico di Torino

where R_f, u', and L_T are flame radius, turbulent intensity, and turbulent length scale, respectively. C_{TFS} and C_{FKG} are two coefficients that can be optimized to tune the flame velocity and to adjust the initial growth rate of the flame kernel, respectively. Equation 6 was modified introducing an explicit pressure dependency in the C_{TFS} coefficient, essential for hydrogen-air flames [65]. All the turbulence-related quantities required by the SITurb are evaluated by a phenomenological 0D turbulence model developed by Gamma Technologies [66]. The turbulence model, which is based on the K-k-eps approach, has been calibrated considering two operating conditions at different engine speeds. The optimization of the model calibration parameters by means of Genetic Algorithm (GA) has allowed the minimization of both the mass averaged integral length scale and Turbulent Kinetic Energy (TKE) deviations with respect to outcomes from 3D-CFD "cold-flow" analysis (i.e., without simulating the combustion process). A good agreement between the 3D-CFD analysis and the calibrated 0D turbulence model was obtained as shown in Figure 6, in

FIGURE 6 Results of 0D turbulence model (in red) compared to 3D-CFD results (in blue) at ST for a high speed-high load and low speed-low load operating conditions: (a) TKE comparison; (b) turbulence length scale comparison.
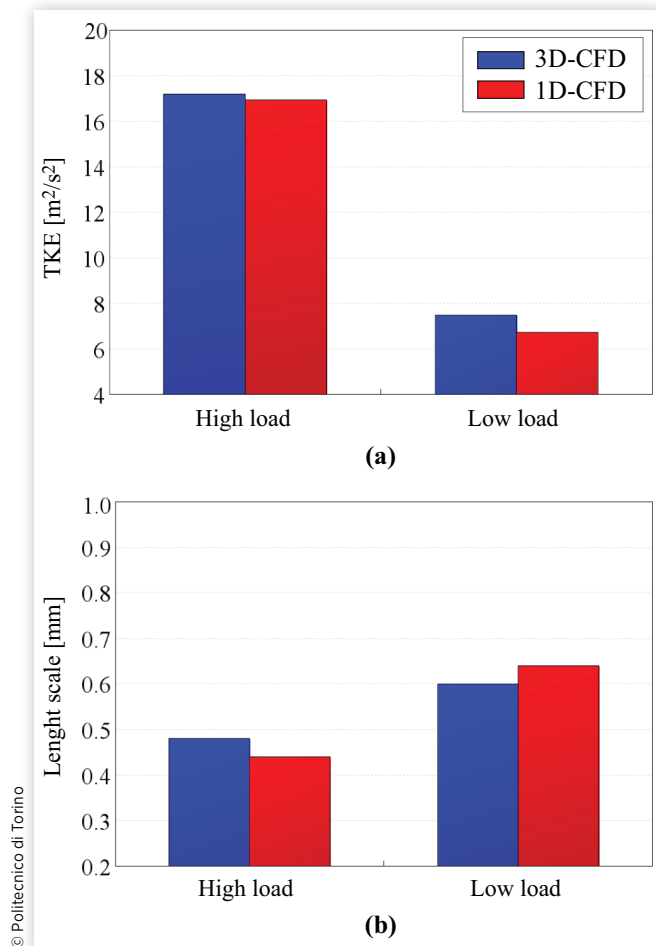
which the TKE and length scale levels for both operating conditions at the related ST are reported.

Once both the laminar flame speed model and the turbulence model are defined, the SITurb combustion model was calibrated against 3D-CFD results by optimizing the three tuning parameters involved in Equations 3 and 6 by means of the GA optimizer. The 13 investigated operating conditions, reported in Table 3, were considered for the SITurb calibration and validation, featuring engine speed, load, ST, EGR, and lambda variations. A Three Pressure Analysis (TPA) model was exploited for the combustion model calibration: pressure signals together with mixture composition at the intake and exhaust manifolds were imposed as boundary conditions, in line with the methodology adopted for the 3D-CFD simulations. In this way, a perfect match in terms of in-cylinder mixture composition and thermodynamic conditions at IVC between the 3D-CFD analysis and the 1D-CFD results were obtained, thus confirming the reliability of the proposed multidimensional synergetic simulation methodology. The above-mentioned match between 3D- and 1D-CFD boundary conditions has allowed a consistent comparison between the HRR evaluated with the 3D-CFD analysis and the one predicted by the SITurb combustion model, whose deviation was minimized during the calibration activity. A comparison between the 3D-CFD and the predicted 1D-CFD in-cylinder pressure (solid) and burn rate (dashed) profiles at low- and high-load conditions is given in Figure 7.

The correlated combustion model is able to faithfully simulate the combustion process leading to limited deviation from the 3D-CFD burn rate and in-cylinder pressure. Moreover, the effect of different mixture dilutions (combining both equivalence ratio and EGR content variation) is properly captured by the SITurb combustion model at low-load engine conditions, as depicted in Figures 7(a) and 7(b). Finally, the predictive capabilities of the combustion model are preserved at higher engine loads [Figure 7(c)]. Indeed the combustion process is reproduced with a high accuracy level even retarding the ST as necessary to avoid abnormal combustion phenomena. The satisfactory agreement achieved by the SITurb combustion model is confirmed extending the validation to the whole test matrix as shown by the correlation plots in Figure 8, in which combustion parameters from 1D- and 3D-CFD simulation results are compared. The combustion anchor angle (top left) and duration (top right) are properly predicted by the combustion model achieving an average error lower than 3 deg. The same accuracy is reached for maximum pressure (avg. error lower than 5 bar) and its location in the engine cycle (avg. error lower than 3 deg).

As it is possible to notice from Figure 8, the developed SITurb combustion model is able to reproduce with satisfactory accuracy level the combustion process of the PFI SI hydrogen engine. Nevertheless, for a complete investigation of the H_2 engine potential, NOx emissions should be further considered. To this aim, the SITurb combustion model was finally coupled with the NOx emissions model available in GT-SUITE, based on the Extended Zeldovich Mechanism (EZM) [67]. The NOx model was calibrated and validated against the results of the 3D-CFD investigations thanks to the

FIGURE 7 Pressure and burn rate from 3D-CFD analysis and 0D/1D-CFD predictive combustion model at (a, b) 2000 RPM × 2 bar BMEP considering low (a) and high (b) dilution rate and at (c) 3500 RPM × 10 bar BMEP.
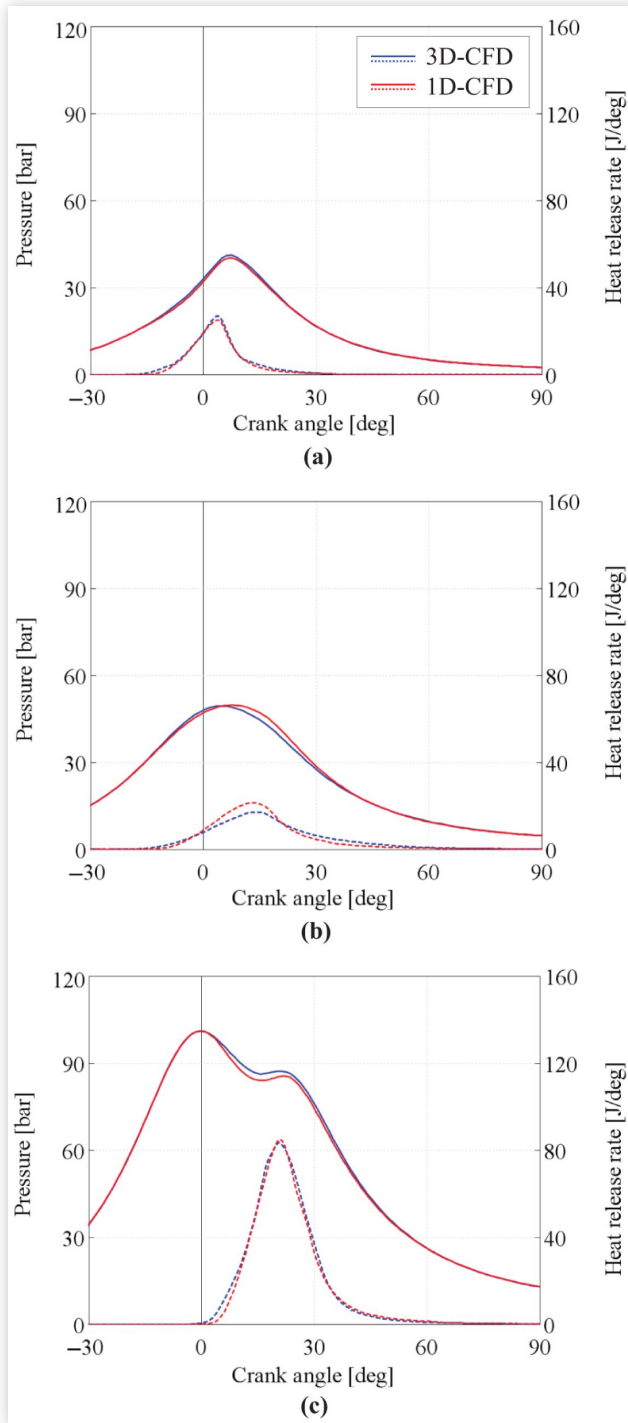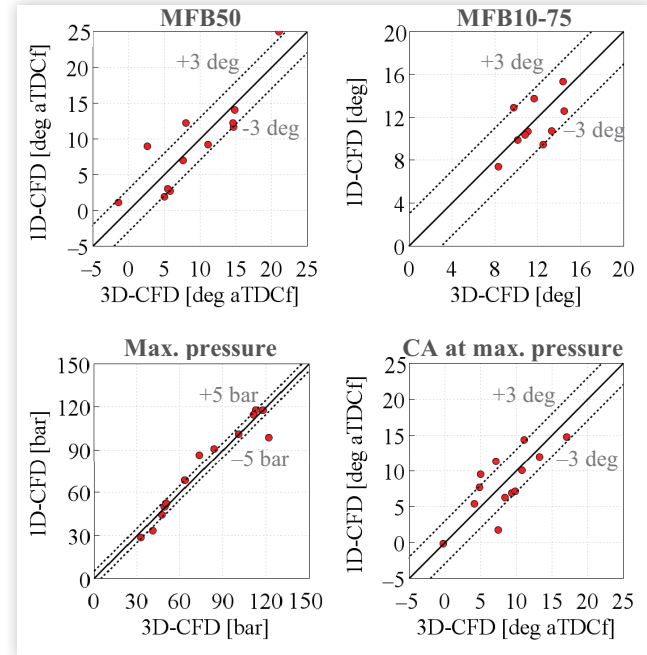

(a)

(b)

(c)

© Politecnico di Torino

FIGURE 8 Correlation plot between 1D-CFD predictions and reference 3D-CFD results: combustion anchor MFB50 (top left), combustion duration MFB10-75 (top right), maximum in-cylinder pressure (bottom left), and crank angle at maximum in-cylinder pressure (bottom right).

© Politecnico di Torino

effects of lambda, EGR, ST, and boost pressure are captured by the EZM with good accuracy, as shown in Figure 9.

Knock Risk Evaluation The same properties that make hydrogen such a desirable fuel for SI ICEs are also responsible for the risk of abnormal combustion even considering the higher Research Octane Number (RON) with respect to common fuels (i.e., RON > 130) [7]. Indeed the wide flammability limits, the low required ignition energy, and the high flame speed can result in the autoignition of the unburned mixture, a prime limitation that needs to be avoided while maintaining acceptable performance. Therefore, a robust methodology of the knock risk is of paramount importance to preliminarily evaluate the impact of H_2 usage in ICEs.

The literature on the knock modelling considering H_2 as a fuel is quite limited. Li and Karim in [35] have proposed a knock criterion comparing the energy released by end-gas reactions to the energy released by the normal flame propagation. However, most of the authors [70, 71] have computed the prediction of knock occurrence by adopting the approach proposed by Livengood and Wu [72], in which the self-ignition of the end gas occurs when

$$\int_{t_{IVC}}^{t_{knock}} \frac{1}{\tau} dt = 1 \qquad \text{Eq. (7)}$$

where τ is the induction time of the air-fuel mixture while t_{IVC} and t_{knock} are the time instants corresponding to the intake valve closing and the autoignition of the unburned gas,

N2 oxidation kinetic scheme embedded in the adopted Zhang et al. mechanism. The results of the optimized NOx model show an average error of 8% in comparison with 3D-CFD results, and a maximum error that lies in the ±20% tolerance band, in line with similar simulation studies [68, 69]. The

FIGURE 9 Results of EZM implemented in the SITurb combustion model against 3D-CFD NOx prediction for five operating conditions.
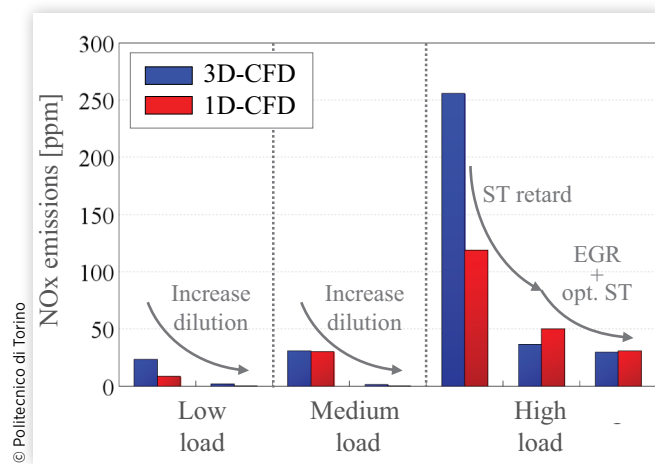

respectively. As far as induction time calculation is concerned, usually it has been relied on phenomenological formulations [73, 74] originally developed for gasoline mixtures. However, these approaches require the RON of the fuel, whose determination with the conventional ASTM method is difficult for hydrogen [70]. Therefore, for this preliminary analysis, an alternative approach has been proposed. The self-ignition times were computed through 0D chemical reactor simulations in the CONVERGE environment through which the time-dependent equations that govern the evolution of chemical and thermodynamic states of an air-fuel mixture were solved, simulating its exothermal reaction in a constant-volume bomb. The time required to observe a temperature increase of 400 K from its initial value was defined as induction time. Such calculations were carried out covering a wide range of pressure, temperature, air-to-fuel ratio, and residuals content (see Table 4). It is worth pointing out that the approach adopted for this preliminary analysis associates self-ignition with knock occurrence. However, as described in detail by Fandakov [75], autoignition does not necessarily imply knock, especially in the case of hydrogen, thus requiring a more appropriate methodology [76].

Engine Controls for Map Definition At first, a 1D-CFD detailed model of the reference engine was developed. In particular, the turbocharger was described by means of a standard map-based approach while hydrogen injection was performed through a simple injector model connected to the intake runners. As far as combustion is concerned, the abovementioned predictive SITurb was adopted. Knock occurrence was accomplished through a chemical approach based on the work carried out by Livengood and Wu, while the heat transfer estimation was relied on the Woschni correlation [77]. Afterwards the complete engine model was exploited to perform a preliminary optimization of the main calibration parameters, such as ST, boost pressure, equivalence ratio, and EGR percentage, over the entire engine operating map.

The optimal calibration strategy at a specific operating condition has to deal with several constraints, such as knock, compressor surge and speed margins, maximum boost temperature (T2) and maximum in-cylinder pressure, turbine inlet pressure (P3), and temperature (T3), required to limit thermal and mechanical stresses of the engine and its subcomponents. In the herein study, an additional threshold of 0.4 g/kWh was set for the Brake-Specific Nitrogen Oxides (BSNOx), in order to comply with the Euro VI limit for HD engines with a reasonable margin [78]. Based on these limitations, a set of Proportional-Integral-Derivative (PID) controllers were employed: a first PID acted on the turbine rack position to reach the target load level and to simultaneously satisfy the constraints on the turbocharger (i.e., avoiding surge and limiting shaft speed), T2, P3, and T3. Contemporarily, a second PID tuned the ST until either the Knock Induction Time Integral (KITI) or the BSNOx limit was reached. Eventually, for each operating point, a Design of Experiments (DoE) methodology [79] was adopted for the selection of the optimal combination of lambda and EGR percentage to maximize the Brake Thermal Efficiency (BTE). According to [7, 10, 80], a minimum lambda equal to 2.1 was considered in order to limit NOx emissions, while values beyond 2.6 were not explored due to the risk of combustion instabilities. As far as EGR is concerned, a maximum value of 30% was investigated, in line with [25]. An example of the results obtained through this methodology is reported in Figure 10, which shows the BTE for different combinations of ST and lambda as a function of KITI and BSNOx for the operating point 3500 RPM × 8 bar BMEP considering two EGR levels, 0% [Figure 10(a)] and 5% [Figure 10(b)]. It is worth pointing out that a sweep of ST for each lambda value is reported to highlight the impact of combustion phasing on engine BTE. Indeed, the above-described methodology identifies for each lambda the optimal value of ST within the useful region of the KITI-BSNOx plane.

As noticeable in Figure 10(a), the maximum BTE area is located in correspondence with the operating points with an advanced combustion phase and a high dilution rate. The adoption of low mixture dilution (i.e., lambda < 2.2) shortens the burn duration with a consequent increase of both in-cylinder peak temperature and NOx emissions. Therefore, to keep BSNOx under control, a retarded ST could be adopted with a delay of the combustion anchor angle, thus lowering the thermodynamic efficiency. On the other hand, the exploitation of leaner lambda implies a decrease of heat transfer and pumping losses as well as a reduction of the in-cylinder peak temperature: this, in addition to limiting NOx formation, allows to reduce the knock likelihood, thus enabling more advanced ST. Nevertheless, an excessive mixture dilution (i.e., lambda > 2.5) implies a severe increase of burn duration, which has a detrimental effect on thermodynamic efficiency despite allowing the adoption of earlier ST. For these reasons, the maximum of engine BTE in the useful region of the KITI-BSNOx plane can be achieved with a lambda value between 2.4 and 2.5. Concerning the exploitation of higher EGR content, as shown in Figure 10(b), this solution has not been

FIGURE 10 BTE obtained with different combinations of ST and lambda as a function of KITI and BSNOx for the operating point 3500 RPM × 8 bar BMEP (a) EGR 0% and (b) EGR 5%.
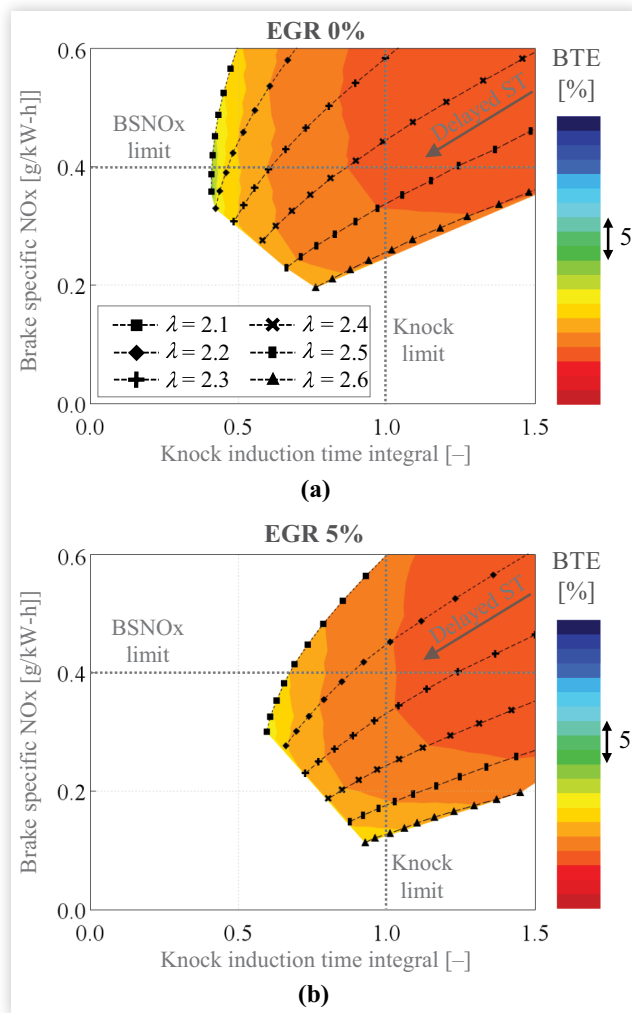
© Politecnico di Torino

found suitable for the selected operating point: indeed the EGR implied an increment of the in-cylinder temperature, which, in turn, leads to a higher knock likelihood, thus requiring a more delayed combustion, with a detrimental effect on the BTE.

Discussion

In this section, the results of the preliminary calibration activity to assess the potential of the H₂-ICE, retrofitted from an existing diesel engine, are presented in terms of complete engine maps. The main engine parameters are reported in Figure 11, including engine efficiency, specific NOx emissions, calibration parameters (setpoint of lambda and EGR ratio and ST), combustion results (anchor angle MFB50 and burn duration MFB10-90), and temperature of the gas at the turbine outlet to preliminarily evaluate the available energy at the inlet of aftertreatment system, not considered in this analysis.

Starting from the full-load performance analysis, a maximum BMEP of 14 bar at 2500 RPM, and a maximum power density of 34 kW/L were achieved with the retrofitted diesel architecture. The full-load curve is mainly limited by the maximum boost pressure, which can be provided by the original turbocharger system, which was proven to be crucial in the case of PFI hydrogen engines, due to the high dilution level required by the hydrogen combustion and to the poor volumetric efficiency that can be achieved with the gaseous injection in the intake ports. Moreover, the retarded ST, exploited as a countermeasure to reduce the knock likelihood induced by the high compression ratio, leads to a significant engine efficiency worsening at high load, thus reducing the engine output. For these reasons, focusing on the Low-End Torque (LET) region, the BMEP resulted to be limited to 5 bar at 1000 RPM and 9 bar at 1500 RPM. Moving to higher engine speeds, a maximum BMEP of 11.5 bar was achieved at 3500 RPM. Decreasing the engine load, the ST was advanced in order to increase the engine efficiency thanks to the higher knock margin, complying at the same time with the NOx constraint. The advanced ST consequently leads to an MFB50 close to the optimum level of 8-10 deg after Top Dead Center firing (aTDCf) and to a reduced combustion duration. Indeed, a wide high-BTE area was achieved with a maximum level of 41% at 2500 RPM × 8 bar BMEP. Finally, moving to the low-load engine region, both lambda and EGR have been increased. On one side, the larger dilution of the mixture induces a slower and less efficient combustion process, while on the other side it provides benefits in terms of heat transfer reduction (due to the lower in-cylinder temperature) and pumping losses decrease (de-throttling effect) achieving the simultaneous minimization of both NOx and fuel consumption. Nevertheless, the adoption of a large dilution level in the low-load engine region leads to low temperature levels downstream of the turbocharger (T4 temperature), and it could represent a relevant challenge for the performance of the aftertreatment system.

Compression Ratio Sensitivity Analysis

As previously pointed out, the baseline diesel compression ratio was found to be quite penalizing—as expected especially at high loads—in terms of acceptable intake manifold pressure and ST due to a severe knock tendency, even considering the high-octane number of hydrogen (RON > 130). To evaluate the potential benefit of a compression ratio reduction in terms of engine efficiency and power output, a sensitivity analysis was conducted by exploiting the correlated 1D-CFD engine model. The results of this study are shown in Figure 12, in which ST, combustion anchor MFB50, power density, and BTE are depicted as a function of compression ratio.

The reduction of the compression ratio from the baseline diesel engine one enables a significant ST advance (more than 10 degrees when the lowest compression ratio is adopted) thanks to the lower mixture temperature during compression, thus leading to a combustion anchor angle MFB50 of +15 deg

FIGURE 11 H$_2$-ICE maps of (a) BTE, (b) BSNOx, (c) lambda, (d) EGR, (e) ST, (f) combustion anchor angle, (g) burn duration (10-90%), and (h) turbine outlet temperature (T4).
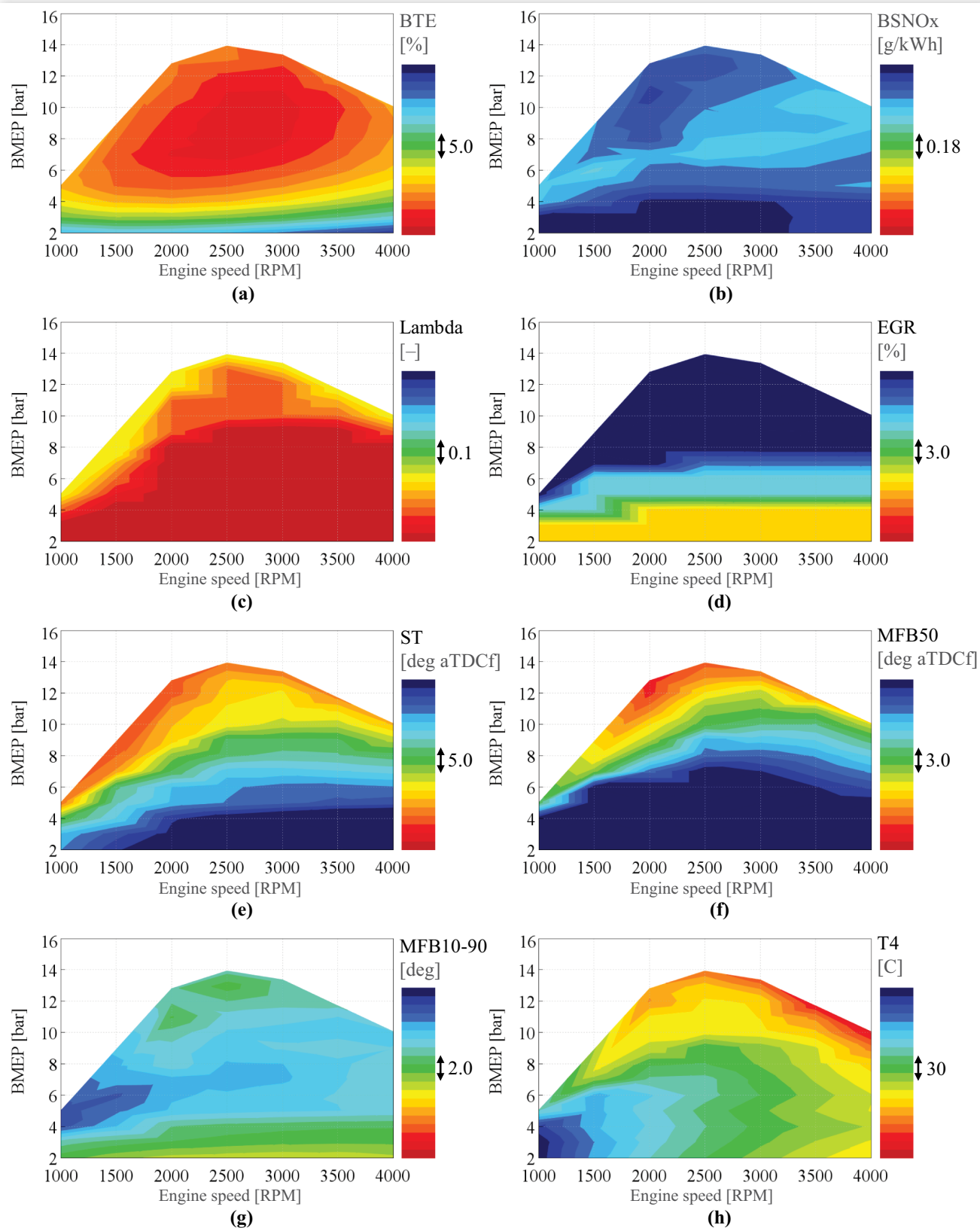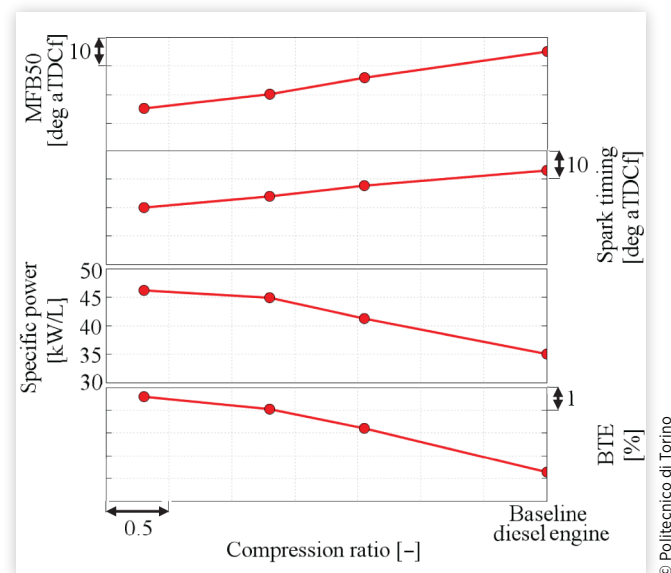
FIGURE 12 ST, combustion anchor angle, power density, and BTE at different compression ratios for the retrofit configuration at rated power.

© Politecnico di Torino

FIGURE 13 (a) BMEP and (b) specific power obtained at full load with a lambda of 2.3 and EGR 0% for different levels of SF.


(a)

(b)

© Politecnico di Torino

aTDCf at rated power, 20 deg advanced with respect to baseline one. This benefit is linked not only to the higher knock margin but also to the reduced combustion duration, thanks to a more favorable spark phasing. Therefore, the advanced and faster combustion process results not only in +2.5% in terms of overall engine efficiency but also in +11 kW/L power density increment. Further investigation should be carried out since at partial load engine operating conditions a reduction of the compression ratio could be detrimental in terms of BTE.

Turbomatching Potential

As above-described, the maximum LET is strongly limited by the turbocharger system that is not able to provide sufficient pressure ratio to compensate for the poor volumetric efficiency due to low-density hydrogen injected in the intake ports. Therefore, to guarantee the high lambda level required to keep knock under control without jeopardizing the LET, a proper turbomatching was carried out starting from the baseline compressor and turbine maps and scaling them through the approach proposed by Ernst et al. [81]. Firstly, a scaling factor (SF) was defined as the ratio between the scaled and the baseline compressor diameter. Afterwards, in accordance with similarity laws [82], the corrected mass flow rate of both compressor and turbine maps was scaled proportionally to the square of the SF, while the baseline-corrected rotational speed was multiplied by 1/SF. On the other hand, efficiency and pressure ratio were kept constant. The results of the adoption of different SFs are reported in Figure 13.

The adoption of a turbocharger with a 40% smaller size (SF = 0.6) guarantees a remarkable increment of the LET, more than doubling the original power output at 1250 RPM. Albeit this implies a severe delay of the combustion anchor angle due to the
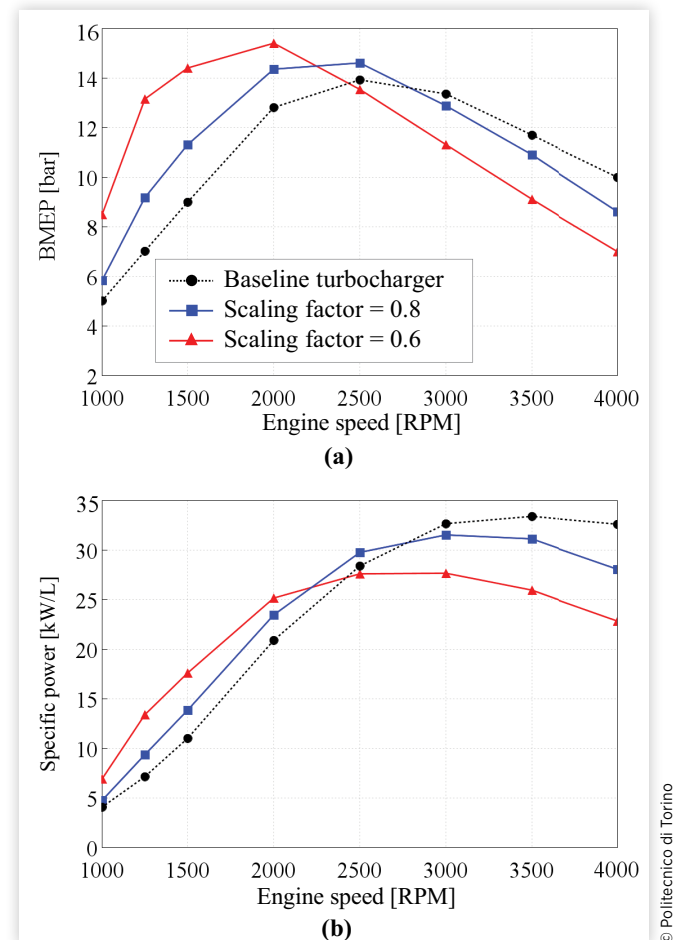
higher boost pressure that raised the knock tendency, as well as an increase of the turbine backpressure, the exhaust gas temperature never exceeds the predefined threshold thanks to the lean conditions of the mixture. The marked increment of LET, however, is paid with a reduction of the peak power, which moves from 34 kW/L at 3500 RPM to 27 kW/L at 3000 RPM. Therefore, a more suitable solution is represented by a 20% smaller turbocharger (SF = 0.8), which allows a significant increase of LET (+20% at 1250 RPM) with an acceptable reduction of the specific power (31 kW/L at 3000 RPM). In general, the above-described results highlight the need to optimize the turbocharger system when passing from a DI diesel engine to a PFI H_2 one due to the different requirements linked to the specific application. A proper turbomatching can allow to increase the LET performance without worsening the power output.

Conclusions

This article presented a comprehensive methodology based on the synergetic use of 0D/1D/3D-CFD numerical simulations to assess the performance of a new generation of

hydrogen propelled engine, retrofitted from an existing state-of-the-art low compression ratio diesel architecture.

3D-CFD simulations relying on a detailed chemistry approach have been used to analyze the H_2 combustion process and have proven their capabilities to catch the effects of both ST and charge dilution. Then the burn rates obtained at this stage of the proposed methodology have been used to calibrate a phenomenological combustion model integrated in a 1D-CFD engine model. The results of this virtual test rig showed a very good agreement with the reference set by the 3D simulations over a wide range of operating conditions and, in particular, when a variation of the engine speed/load and the charge dilution has been performed. Also the prediction of the NOx emissions, which is based on the EZM, showed acceptable errors with respect to the 3D values and similar sensitivity to the engine calibration parameters. As a result, this simulation platform was used to optimize the main operating parameters (e.g., lambda, EGR, and ST) of the engine in order to maximize its thermal efficiency, ensuring it at the same time, NOx emission below the current EU6 limit for HD applications. Finally, the capabilities of the model to drive the design of the engine architecture (e.g., compression ratio and turbocharger size) were assessed.

The main findings of the optimization process of the revamped diesel engine can be summarized as follow:

- The 3D-CFD simulations proved the effectiveness of H_2O_2 as a marker for the H_2 flame propagations and show the significant reduction of the combustion speed related to the use of high EGR levels.

- The phenomenological combustion model integrated into the 1D virtual test rig shows a good agreement with the detailed 3D simulations not only in terms of combustion parameters but also in terms of NOx emissions.

- The optimization process carried out on the engine operating parameter allows achieving a peak efficiency of about 41% ensuring, at the same time, the achievement of the constraint on the NOx emission and a satisfactory specific power level (34 kW/L).

- The reduction of compression ratio enables a further increase in both the efficiency (+3%) and the performance (+10 kW/L) of the engine.

- An optimization of the turbomatching may enable an increase of about 30% in the LET of the engine with an acceptable reduction of its specific power (31 kW/L).

Once validated the proposed methodology against experiments, future research activities will be focused on different engine configurations (e.g., Direct Injections, DI+PFI) and advanced combustion concepts (e.g., Turbulent Jet Ignition—TJI) in order to assess their benefits on the performance of future H_2-ICEs.

Acknowledgments

Contact Information

Prof. Federico Millo
Politecnico di Torino—Energy Department
C.so Duca degli Abruzzi, 24
10129 Turin, Italy
federico.millo@polito.it
www.polito.it/engines

Abbreviations

AMR - Adaptive Mesh Refinement

aTDCf - After Top Dead Center firing

BMEP - Brake Mean Effective Pressure

BSNOx - Brake-Specific Nitrogen Oxides

BTE - Brake Thermal Efficiency

CAC - Charge Air Cooler

CFD - Computational Fluid Dynamics

CPU - Central Processing Unit

CR - Common Rail

DI - Direct Injection

DoE - Design of Experiments

EGR - Exhaust Gas Recirculation

EU - European Union

EZM - Extended Zeldovich Mechanism

FC - Fuel Cell

GA - Genetic Algorithm

GHG - Greenhouse Gases

HD - Heavy Duty

HRR - Heat Release Rate

ICE - Internal Combustion Engine

KITI - Knock Induction Time Integral

Lambda - Relative air-to-fuel ratio

LET - Low-End Torque

LHV - Lower Heating Value

MFB10-75 - 10-75% Mass Fuel Burned angle

MFB10-90 - 10-90% Mass Fuel Burned angle

MFB50 - 50% Mass Fuel Burned angle

NOx - Nitrogen Oxides

P3 - Turbine inlet pressure

PFI - Port Fuel Injection

PID - Proportional-Integral-Derivative

PISO - Pressure Implicit with Splitting Operator

RANS - Reynolds-Averaged Navier-Stokes

RNG - Re-Normalization Group

RON - Research Octane Number

SF - Scaling Factor

SI - Spark Ignition

ST - Spark Timing

T2 - Boost temperature

T3 - Turbine inlet temperature

T4 - Turbine outlet temperature

TJI - Turbulent Jet Ignition

TKE - Turbulent Kinetic Energy

TPA - Three Pressure Analysis

VGT - Variable Geometry Turbine

WSR - Well-Stirred Reactor

References

1. European Commission, "Communication from the Commission the European Green Deal," COM/2019/640 Final, Brussels, 2019, accessed July 2021, https://eur-lex.europa.eu/legal-content/EN/TXT/?uri=COM%3A2019%3A640%3AFIN.

2. Korn, T., "Der effizienteste Weg zur CO$_2$-Minderung: die neueste Generation von Wasserstoffverbrennungsmotoren [The Most Efficient Way for CO$_2$ Reduction: The New Generation of Hydrogen Internal Combustion Engines Summary]," in *41th International Vienna Motor Symposium*, Vienna, 2020.

3. Dilara, P., "The Future of Clean Cars in Europe: EU Green Deal and EURO 7," in *4th Sino-EU Workshop on New Emissions Standards and Regulations for Motor Vehicles*, Virtual event jointly organised by the Vehicle Emission Control Center (China) and the Joint Research Centre, 2021.

4. European Commission, "Communication from the Commission to the European Parliament, the Council, the European Economic and Social Committee and the Committee of the Regions a Hydrogen Strategy for a Climate-Neutral Europe," COM/2020/301 Final, Brussels, 2020, accessed July 2021, https://eur-lex.europa.eu/legal-content/EN/TXT/?qid=1594897267722&uri=CELEX:52020DC0301.

5. European Commission, "European Clean Hydrogen Alliance," 2020, accessed July 2021, https://ec.europa.eu/growth/industry/policy/european-clean-hydrogen-alliance_en.

6. Manoharan, Y., Hosseini, S.E., Butler, B., Alzhahrani, H. et al., "Hydrogen Fuel Cell Vehicles: Current Status and Future Prospect," *Applied Sciences* 9, no. 11 (2019): 2296, https://doi.org/10.3390/app9112296.

7. Yip, H.L., Srna, A., Yuen, A.C.Y., Kook, S. et al., "A Review of Hydrogen Direct Injection for Internal Combustion Engines: Towards Carbon-Free Combustion," *Applied Sciences* 9, no. 22 (2019): 4842, https://doi.org/10.3390/app9224842.

8. Munshi, S., Garner, G., Theissl, H., Hofer, F. et al., "Total Cost of Ownership (TCO) Analysis for Heavy Duty Hydrogen Fueled Powertrains," 2021, accessed July 2021, https://wfsinc.com/file_library/files/wpt-wfsinc/20201225_Westport_AVL_Whitepaper_Hydrogen_HPDI_final.pdf.

9. Verhelst, S., Demuynck, J., Sierens, R., Scarcelli, R. et al., "Chapter 16—Update on the Progress of Hydrogen-Fueled Internal Combustion Engines," in: *Renewable Hydrogen Technologies* (Elsevier, 2013), 381-400, https://doi.org/10.1016/B978-0-444-56352-1.00016-7.

10. Karim, G.A., "Hydrogen as a Spark Ignition Engine Fuel," *International Journal of Hydrogen Energy* 28, no. 5 (2003): 569-577, https://doi.org/10.1016/S0360-3199(02)00150-7.

11. Jilakara, S., Vaithianathan, J., Natarajan, S., Ramakrishnan, V. et al., "An Experimental Study of Turbocharged Hydrogen Fuelled Internal Combustion Engine," *SAE Int. J. Engines* 8, no. 1 (2015): 314-325, https://doi.org/10.4271/2015-26-0051.

12. Berckmüller, M., Rottengruber, H., Eder, A., Brehm, N. et al., "Potentials of a Charged SI-Hydrogen Engine," SAE Technical Paper 2003-01-3210, 2003, https://doi.org/10.4271/2003-01-3210.

13. Klepatz, K., Rottengruber, H., Zeilinga, S., Koch, D. et al., "Loss Analysis of a Direct-Injection Hydrogen Combustion Engine," SAE Technical Paper 2018-01-1686, 2018, https://doi.org/10.4271/2018-01-1686.

14. Dhyani, V. and Subramanian, K.A., "Fundamental Characterization of Backfire in a Hydrogen Fuelled Spark Ignition Engine Using CFD and Experiments," *International Journal of Hydrogen Energy* 44, no. 60 (2019): 32254-32270, https://doi.org/10.1016/j.ijhydene.2019.10.077.

15. Winkler-Goldstein, R. and Rastetter, A., "Power to Gas: The Final Breakthrough for the Hydrogen Economy?" *Green* 3, no. 1 (2013): 69-78, https://doi.org/10.1515/green-2013-0001.

16. Abdalla, A.M., Hossain, S., Nisfindy, O.B., Azad, A.T. et al., "Hydrogen Production, Storage, Transportation and Key Challenges with Applications: A Review," *Energy Conversion and Management* 165 (2018): 602-627, https://doi.org/10.1016/j.enconman.2018.03.088.

17. Enke, W., Gruber, M., Hecht, L., and Staar, B., "Der bivalente V12-Motor des BMW Hydrogen 7," *MTZ-Motortechnische Zeitschrift* 68 (2007): 446-453, https://doi.org/10.1007/BF03227411.

18. Mazda, "MAZDA: Hydrogen Vehicles," https://www.mazda.com/en/innovation/technology/env/hre/, accessed 02 Dec. 2021.

19. MAN and Shell, "Shell, MAN and Connexxion Planning Worlds Largest Hydrogen Public Transport Project," in *Green Car Congress*, 2006, https://www.greencarcongress.com/2006/06/shell_man_and_c.html, accessed 02 Dec. 2021.

20. Pauer, T., Weller, H., Schünemann, E., Eichlseder, H. et al., "H$_2$ ICE for Future Passenger Cars and Light Commercial Vehicles," in *41th International Vienna Motor Symposium*, Vienna, 2020.

21. Babayev, R., Andersson, A., Dalmau, A.S., Im, H.G. et al., "Computational Characterization of Hydrogen Direct Injection and Nonpremixed Combustion in a Compression-

Ignition Engine," *International Journal of Hydrogen Energy* 46, no. 35 (2021): 18678-18696, https://doi.org/10.1016/j.ijhydene.2021.02.223.

22. Tsujimura, T. and Suzuki, Y., "The Utilization of Hydrogen in Hydrogen/Diesel Dual Fuel Engine," *International Journal of Hydrogen Energy* 42, no. 19 (2017): 14019-14029, https://doi.org/10.1016/j.ijhydene.2017.01.152.

23. Saravanan, N., Nagarajan, G., Sanjay, G., Dhanasekaran, C. et al., "Combustion Analysis on a DI Diesel Engine with Hydrogen in Dual Fuel Mode," *Fuel* 87, no. 17-18 (2008): 3591-3599, https://doi.org/10.1016/j.fuel.2008.07.011.

24. White, C.M., Steeper, R.R., and Lutz, A.E., "The Hydrogen-Fueled Internal Combustion Engine: A Technical Review," *International Journal of Hydrogen Energy* 31, no. 10 (2006): 1292-1305, https://doi.org/10.1016/j.ijhydene.2005.12.001.

25. Thomas Koch, D., Sousa, A., and Bertram, D., "H_2-Engine Operation with EGR Achieving High Power and High Efficiency Emission-Free Combustion," SAE Technical Paper 2019-01-2178, 2019, https://doi.org/10.4271/2019-01-2178.

26. Li, Y., Gao, W., Zhang, P., Ye, Y. et al., "Effects Study of Injection Strategies on Hydrogen-Air Formation and Performance of Hydrogen Direct Injection Internal Combustion Engine," *International Journal of Hydrogen Energy* 44, no. 47 (2019): 26000-26011, https://doi.org/10.1016/j.ijhydene.2019.08.055.

27. Verhelst, S., De Landtsheere, J., De Smet, F., Billiouw, C. et al., "Effects of Supercharging, EGR and Variable Valve Timing on Power and Emissions of Hydrogen Internal Combustion Engines," *SAE Int. J. Engines* 1, no. 1 (2009): 647-656, https://doi.org/10.4271/2008-01-1033.

28. Le Moine, J., Senecal, P.K., Kaiser, S.A., Salazar, V.M. et al., "A Computational Study of the Mixture Preparation in a Direct-Injection Hydrogen Engine," *J. Eng. Gas Turbines Power* 137, no. 11 (2015): 111508, https://doi.org/10.1115/1.4030397.

29. Gerke, U. and Boulouchos, K., "Three-Dimensional Computational Fluid Dynamics Simulation of Hydrogen Engines Using a Turbulent Flame Speed Closure Combustion Model," *International Journal of Engine Research* 13, no. 5 (2012): 464-481, https://doi.org/10.1177/1468087412438796.

30. Scarcelli, R., Wallner, T., Obermair, H., Salazar, V.M. et al., "CFD and Optical Investigations of Fluid Dynamics and Mixture Formation in a DI-H2ICE," in *ASME 2010 Internal Combustion Engine Division Fall Technical Conference*, San Antonio, TX, 2010, https://doi.org/10.1115/ICEF2010-35084.

31. Wallner, T., Matthias, N., and Scarcelli, R., "Influence of Injection Strategy in a High-Efficiency Hydrogen Direct Injection Engine," *SAE Int. J. Fuels Lubr.* 5, no. 1 (2012): 289-300, https://doi.org/10.4271/2011-01-2001.

32. Scarcelli, R., Wallner, T., Matthias, N., Salazar, V. et al., "Mixture Formation in Direct Injection Hydrogen Engines: CFD and Optical Analysis of Single- and Multi-Hole Nozzles," *SAE Int. J. Engines* 4, no. 2 (2011): 2361-2375, https://doi.org/10.4271/2011-24-0096.

33. Verhelst, S., Woolley, R., Lawes, M., and Sierens, R., "Laminar and Unstable Burning Velocities and Markstein

Lengths of Hydrogen-Air Mixtures at Engine-Like Conditions," *Proceedings of Combustion Institute* 30, no. 1 (2005): 209-216, https://doi.org/10.1016/j.proci.2004.07.042.

34. Ó Conaire, M., Curran, H.J., Simmie, J.M., Pitz, W.J. et al., "A Comprehensive Modeling Study of Hydrogen Oxidation," *Int. J. Chem. Kinet.* 36, no. 11 (2004): 603-622, https://doi.org/10.1002/kin.20036.

35. Li, H. and Karim, G.A., "Knock in Spark Ignition Hydrogen Engines," *International Journal of Hydrogen Energy* 29, no. 8 (2004): 859-865, https://doi.org/10.1016/j.ijhydene.2003.09.013.

36. Golisano, I.R., Scalabrini, I.S., Arpaia, A., Pesce, F.C. et al., "PUNCH Hydrogen Internal Combustion Engine & KERS: An Appealing Value-Proposition for Green Power Pack," in *42th International Vienna Motor Symposium*, Vienna, 2021.

37. Richards, K.J., Senecal, P.K., and Pomraning, E., *CONVERGE 3.0.14* (Madison, WI: Convergent Science, 2021)

38. Issa, R.I., "Solution of the Implicitly Discretised Fluid Flow Equations by Operator-Splitting," *Journal of Computational Physics* 62, no. 1 (1986): 40-65, https://doi.org/10.1016/0021-9991(86)90099-9.

39. Rhie, C.M. and Chow, W.L., "Numerical Study of the Turbulent Flow Past an Airfoil with Trailing Edge Separation," *AIAA Journal* 21, no. 11 (1983): 1525-1532, https://doi.org/10.2514/3.8284.

40. Convergent Science, "CONVERGE Manual v3.0," 2020.

41. Scarcelli, R., Matthias, N., and Wallner, T., "Numerical Investigation of Combustion in a Lean Burn Gasoline Engine," SAE Technical Paper 2013-24-0029, 2013, https://doi.org/10.4271/2013-24-0029.

42. Orszag, S.A., Yakhot, V., Flannery, W.S., Boysan, F. et al., "Renormalization Group Modeling and Turbulence Simulations," in: *Near-Wall Turbulent Flows* (1993), 1031-1046.

43. Yakhot, V., Orszag, S.A., Thangam, S., and Gatski, T.B., "Development of Turbulence Models for Shear Flows by a Double Expansion Technique," *Physics of Fluids A: Fluid Dynamics* 4 (1992): 1510, https://doi.org/10.1063/1.858424.

44. Versteeg, H.K. and Malalasekera, W., *An Introduction to Computational Fluid Dynamics: The Finite Volume Method* (Harlow: Prentice Hall, 2007)

45. Amsden, A.A., "KIVA-3V: A Block-Structured KIVA Program for Engines with Vertical or Canted Valves," 1997, https://doi.org/10.2172/505339.

46. Givler, S., Raju, M., Pomraning, E., Senecal, P. et al., "Gasoline Combustion Modeling of Direct and Port-Fuel Injected Engines Using a Reduced Chemical Mechanism," SAE Technical Paper 2013-01-1098, 2013, https://doi.org/10.4271/2013-01-1098.

47. Broatch, A., Margot, X., Novella, R., and Gomez-Soriano, J., "Combustion Noise Analysis of Partially Premixed Combustion Concept Using Gasoline Fuel in a 2-Stroke Engine," *Energy* 107 (2016): 612-624, https://doi.org/10.1016/j.energy.2016.04.045.

48. Battistoni, M., Mariani, F., Risi, F., and Poggiani, C., "Combustion CFD Modeling of a Spark Ignited Optical

Access Engine Fueled with Gasoline and Ethanol," *Energy Procedia* 82 (2015): 424-431, https://doi.org/10.1016/j.egypro.2015.11.829.

49. Biswas, S., *Physics of Turbulent Jet Ignition: Mechanisms and Dynamics of Ultra-Lean Combustion* (Springer International Publishing, 2018), https://doi.org/10.1007/978-3-319-76243-2.

50. Savard, B. and Blanquart, G., "An a Priori Model for the Effective Species Lewis Numbers in Premixed Turbulent Flames," *Combustion and Flame* 161 (2014): 1547-1557, https://doi.org/10.1016/j.combustflame.2013.12.014.

51. Zhang, Y., Mathieu, O., Petersen, E.L., Bourque, G. et al., "Assessing the Predictions of a NOx Kinetic Mechanism on Recent Hydrogen and Syngas Experimental Data," *Combustion and Flame* 182 (2017): 122-141, https://doi.org/10.1016/j.combustflame.2017.03.019.

52. Kéromnès, A., Metcalfe, W.K., Heufer, K.A., Donohoe, N. et al., "An Experimental and Detailed Chemical Kinetic Modeling Study of Hydrogen and Syngas Mixture Oxidation at Elevated Pressures," *Combustion and Flame* 160 (2013): 995-1011, https://doi.org/10.1016/j.combustflame.2013.01.001.

53. Olm, C., Zsély, I.G., Pálvölgyi, R., Varga, T. et al., "Comparison of the Performance of Several Recent Hydrogen Combustion Mechanisms," *Combust. Flame* 161 (2014): 2219-2234, https://doi.org/10.1016/j.combustflame.2014.03.006.

54. Lemke, M., Cai, L., Reiss, J., Pitsch, H. et al., "Adjoint-Based Sensitivity Analysis of Quantities of Interest of Complex Combustion Models," *Combustion Theory and Modelling* 23 (2019): 180-196, https://doi.org/10.1080/13647830.2018.1495845.

55. Alam, S.S. and Depcik, C., "Adaptive Wiebe Function Parameters for a Port-Fuel Injected Hydrogen-Fueled Engine," in *Proceedings of ASME International Mechanical Engineering Congress and Exposition IMECE2019*, Salt Lake City, UT, 2019, https://doi.org/10.1115/IMECE2019-10031.

56. Kunal, R., Natarajan, S., Abraham, M., Subash, G. et al., "Effects of Governing Parameters on the Performance and Emissions of Hydrogen Engine for Automotive Application," SAE Technical Paper 2013-01-2891, 2013, https://doi.org/10.4271/2013-01-2891.

57. Rezaei, R., Hayduk, C., Sens, M., Fandakov, A., et al., "Hydrogen Combustion—A Puzzle Piece of Future Sustainable Transportation!," in *Proceedings of SIA 2020 Digital Powertrain & Energy*, France, 2020, 304-311.

58. D'Errico, G., Onorati, A., and Ellgas, S., "1D Thermo-Fluid Dynamic Modelling of an S.I. Single-Cylinder H_2 Engine with Cryogenic Port Injection," *International Journal of Hydrogen Energy* 33, no. 20 (2008): 5829-5841, https://doi.org/10.1016/j.ijhydene.2008.05.096.

59. Mirzaeian, M., Millo, F., and Rolando, L., "Assessment of the Predictive Capabilities of a Combustion Model for a Modern Downsized Turbocharged SI Engine," SAE Technical Paper 2016-01-0557, 2016, https://doi.org/10.4271/2016-01-0557.

60. Millo, F., Gullino, F., and Rolando, L., "Methodological Approach for 1D Simulation of Port Water Injection for Knock Mitigation in a Turbocharged DISI Engine," *Energies* 13, no. 17 (2020): 1-21, https://doi.org/10.3390/en13174297.

61. Wahiduzzaman, S., Moral, T., and Sheard, S., "Comparison of Measured and Predicted Combustion Characteristics of a Four-Valve S.I. Engine," SAE Technical Paper 930613, 1993, https://doi.org/10.4271/930613.

62. Zhang, K., Banyon, C., Bugler, J., Curran, H.J. et al., "An Updated Experimental and Kinetic Modeling Study of *n*-Heptane Oxidation," *Combustion and Flame* 172 (2016): 116-135, https://doi.org/10.1016/j.combustflame.2016.06.028.

63. Metghalchi, M. and Keck, J.C., "Burning Velocities of Mixtures of Air with Methanol, Isooctane, and Indolene at High Pressure and Temperature," *Combustion and Flame* 48 (1982): 191-210, https://doi.org/10.1016/0010-2180(82)90127-4.

64. Verhelst, S., Sierens, R., "A Laminar Burning Velocity Correlation for Hydrogen/Air Mixtures Valid at Spark-Ignition Engine Conditions," in *Proceedings of ICES03 2003 Spring Technical Conference of the ASME Internal Combustion Engine Division*, Salzburg, Austria, 2003, https://doi.org/10.1115/ICES2003-0555.

65. Kitagawa, T., Nakahara, T., Maruyama, K., Kado, K. et al., "Turbulent Burning Velocity of Hydrogen-Air Premixed Propagating Flames at Elevated Pressures," *International Journal of Hydrogen Energy* 33, no. 20 (2008): 5842-5849, https://doi.org/10.1016/j.ijhydene.2008.06.013.

66. Fogla, N., Bybee, M., Mirzaeian, M., Millo, F. et al., "Development of a K-k-ε Phenomenological Model to Predict In-Cylinder Turbulence," *SAE Int. J. Engines* 10, no. 2 (2017): 562-575, https://doi.org/10.4271/2017-01-0542.

67. Lavoie, G.A., Heywood, J.B., and Keck, J.C., "Experimental and Theoretical Study of Nitric Oxide Formation in Internal Combustion Engines," *Combustion Science and Technology* 1, no. 4 (1970): 313-326, https://doi.org/10.1080/00102206908952211.

68. Esposito, S., Diekhoff, L., and Pischinger, S., "Prediction of Gaseous Pollutant Emissions from a Spark-Ignition Direct-Injection Engine with Gas-Exchange Simulation," *International Journal of Engine Research* 22, no. 12 (2021): 3533-3547, https://doi.org/10.1177/14680874211005053.

69. Millo, F., Boccardo, G., Piano, A., Arnone, L. et al., "Numerical Simulation of the Combustion Process of a High EGR, High Injection Pressure, Heavy Duty Diesel Engine," SAE Technical Paper 2017-24-0009, 2017, https://doi.org/10.4271/2017-24-0009.

70. Boretti, A.A. and Watson, H.C., "Enhanced Combustion by Jet Ignition in a Turbocharged Cryogenic Port Fuel Injected Hydrogen Engine," *International Journal of Hydrogen Energy* 34, no. 5 (2009): 2511-2516, https://doi.org/10.1016/j.ijhydene.2008.12.089.

71. Sadiq Al-Baghdadi, M.A.R., "Development of a Pre-ignition Submodel for Hydrogen Engines," *Proceedings of the Institution of Mechanical Engineers, Part D: Journal of Automobile Engineering* 219, no. 10 (2005): 1203-1212, https://doi.org/10.1243/095440705X34883.

72. Livengood, J.C. and Wu, P.C., "Correlation of Autoignition Phenomena in Internal Combustion Engines and Rapid Compression Machines," *Symposium (International) on*

Combustion 5, no. 1 (1955): 347-355, https://doi.org/10.1016/S0082-0784(55)80047-1.

73. Douaud, A. and Eyzat, P., "Four-Octane-Number Method for Predicting the Anti-Knock Behavior of Fuels and Engines," SAE Technical Paper 780080, 1978, https://doi.org/10.4271/780080.

74. Gamma Technologies, "GT-SUITE Engine Performance Manual v2020," 2019.

75. Fandakov, A., *A Phenomenological Knock Model for the Development of Future Engine Concepts* (Springer Vieweg, 2018), https://doi.org/10.1007/978-3-658-24875-8.

76. Bianco, A., Millo, F., and Piano, A., "Modelling of Combustion and Knock Onset Risk in a High-Performance Turbulent Jet Ignition Engine," *Transportation Engineering* 2 (2020): 100037, https://doi.org/10.1016/j.treng.2020.100037.

77. Woschni, G., "A Universally Applicable Equation for the Instantaneous Heat Transfer Coefficient in the Internal Combustion Engine," SAE Technical Paper 670931, 1967, https://doi.org/10.4271/670931.

78. DieselNet, "EU: Heavy-Duty Truck and Bus Engines—Emission Standards," accessed May 2021, https://dieselnet.com/standards/eu/hd.php#intro.

79. Millo, F., Pautasso, E., Delneri, D., and Troberg, M., "A DoE Analysis on the Effects of Compression Ratio, Injection Timing, Injector Nozzle Hole Size and Number on Performance and Emissions in a Diesel Marine Engine," SAE Technical Paper 2007-01-0670, 2007, https://doi.org/10.4271/2007-01-0670.

80. Beatrice, C., "Technology Review for SI ICE Based Powertrains with 50% Brake Thermal Efficiency," Presented at in *Does the Internal Combustion Engine Have a Future? International Workshop*, Torino, 2020.

81. Ernst, B., Kammeyer, J., and Seume, J.R., "Improved Map Scaling Methods for Small Turbocharger Compressors,"

Proceedings of ASME Turbo Expo 3 (2011): 733-744, https://doi.org/10.1115/GT2011-45345.

82. Japikse, D., *Centrifugal Compressor Design and Performance* (Wilder, Vermont: Concepts ETI, 1996)

Appendix A

The laminar flame speed model, described in the manuscript, was developed and correlated against detailed chemistry calculations. The model expression is reported in Equation 4, while each single term of the equation ($S_{L,0}$, α, β, and γ) is described in Equations A.1, A.2, A.3, and A.4, respectively.

$$S_{L,0} = 30.009\,\phi^5 - 87.697\,\phi^4 + 88.628\,\phi^3 - 33.781\,\phi^2 + 5.489\,\phi - 0.301 \qquad \text{Eq. (A.1)}$$
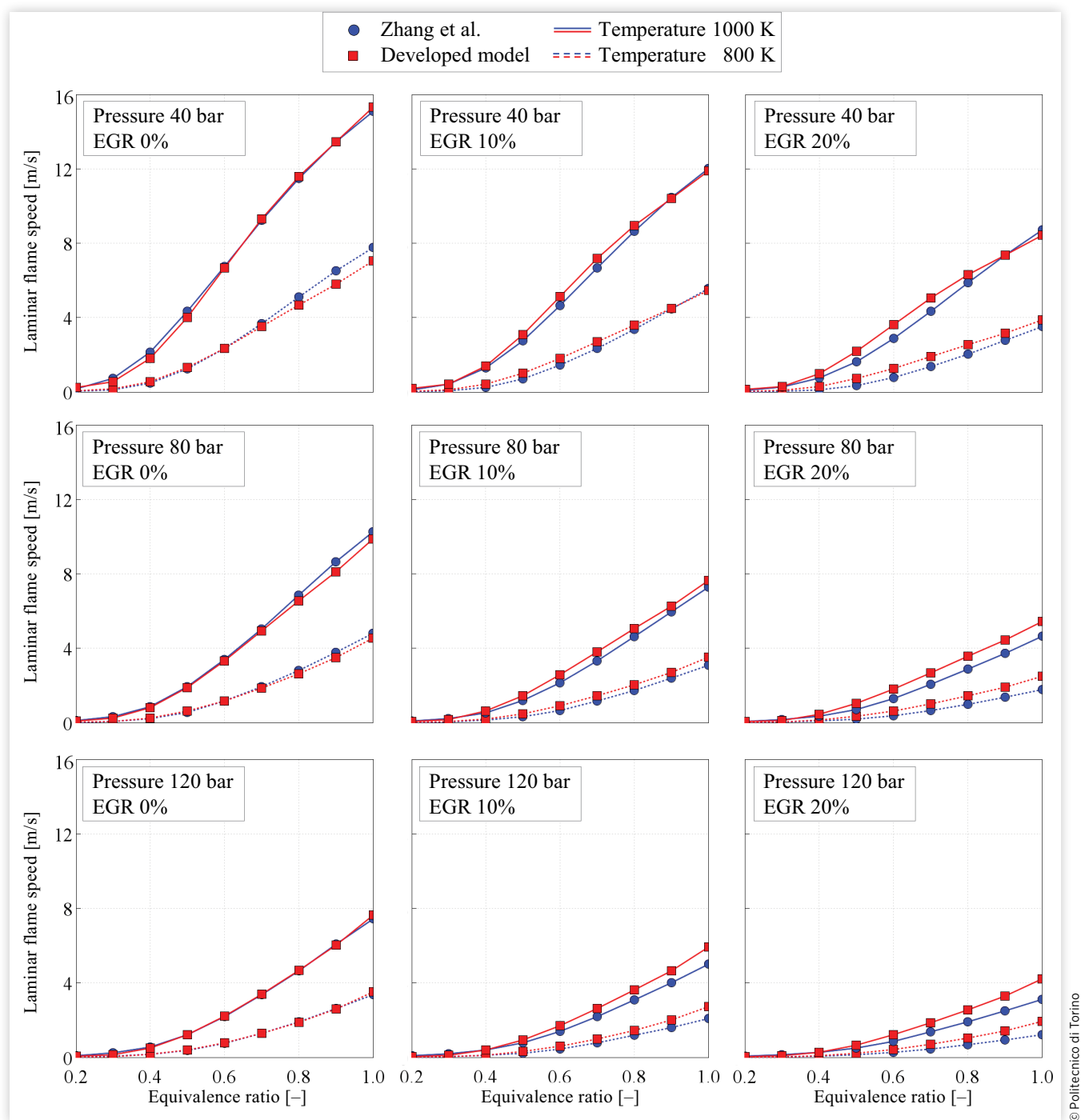
$$\alpha = 0.105\,\phi^2 - 3.135\,\phi + 6.514 \qquad \text{Eq. (A.2)}$$

$$\beta = 0.177\,\phi^2 + 0.636\,\phi - 1.449 \qquad \text{Eq. (A.3)}$$

$$\gamma = -0.306\,\phi^2 + 0.418\,\phi + 2.134 \qquad \text{Eq. (A.4)}$$

In Figure A.1 a comparison between the predicted laminar flame speed values and the results from the 1D-CFD calculations is reported, at different pressure, temperature, and EGR levels. A satisfactory accuracy level can be highlighted from Figure A.1. A slight overprediction of the laminar flame speed at increasing EGR content can be pointed out; however, the maximum deviation from the reference CFD results is always limited to ±20% in the equivalence ratio range of 0.3 ± 0.6 and for EGR ratio lower than 20%.

FIGURE A.1 Hydrogen laminar flame speed computed by means of Zhang et al.'s mechanism and the developed correlation at different equivalence ratios, pressures, unburned temperatures, and EGR percentages.

Positions and opinions advanced in this work are those of the author(s) and not necessarily those of SAE International. Responsibility for the content of the work lies solely with the author(s).